

# Discovery of VHE $\gamma$ -ray emission and multi-wavelength observations of the BL Lac object 1RXS J101015.9–311909

HESS Collaboration, A. Abramowski<sup>1</sup>, F. Acero<sup>2</sup>, F. Aharonian<sup>3,4,5</sup>, A.G. Akhperjanian<sup>6,5</sup>, G. Anton<sup>7</sup>, A. Balzer<sup>7</sup>, A. Barnacka<sup>8,9</sup>, Y. Becherini<sup>10,11</sup>, J. Becker<sup>12</sup>, K. Bernlöhr<sup>3,13</sup>, E. Birsin<sup>13</sup>, J. Biteau<sup>11</sup>, A. Bochow<sup>3</sup>, C. Boisson<sup>14</sup>, J. Bolmont<sup>15</sup>, P. Bordas<sup>16</sup>, J. Brucker<sup>7</sup>, F. Brun<sup>11</sup>, P. Brun<sup>9</sup>, T. Bulik<sup>17</sup>, I. Büsching<sup>18,12</sup>, S. Carrigan<sup>3</sup>, S. Casanova<sup>18,3</sup>, M. Cerruti<sup>14</sup>, P.M. Chadwick<sup>19</sup>, A. Charbonnier<sup>15</sup>, R.C.G. Chaves<sup>9,3</sup>, A. Cheesebrough<sup>19</sup>, G. Cologna<sup>20</sup>, J. Conrad<sup>21</sup>, M. Dalton<sup>13</sup>, M.K. Daniel<sup>19</sup>, I.D. Davids<sup>22</sup>, B. Degrange<sup>11</sup>, C. Deil<sup>3</sup>, H.J. Dickinson<sup>21</sup>, A. Djannati-Atai<sup>10</sup>, W. Domainko<sup>3</sup>, L.O'C. Drury<sup>4</sup>, G. Dubus<sup>23</sup>, K. Dutson<sup>24</sup>, J. Dyks<sup>8</sup>, M. Dyrda<sup>25</sup>, K. Egberts<sup>26</sup>, P. Eger<sup>7</sup>, P. Espigat<sup>10</sup>, L. Fallon<sup>4</sup>, S. Fegan<sup>11</sup>, F. Feinstein<sup>2</sup>, M.V. Fernandes<sup>1</sup>, A. Fiasson<sup>27</sup>, G. Fontaine<sup>11</sup>, A. Förster<sup>3</sup>, M. Füßling<sup>13</sup>, Y.A. Gallant<sup>2</sup>, H. Gast<sup>3</sup>, L. Gérard<sup>10</sup>, D. Gerbig<sup>12</sup>, B. Giebels<sup>11</sup>, J.F. Glicenstein<sup>9</sup>, B. Glück<sup>7</sup>, D. Göring<sup>7</sup>, S. Häffner<sup>7</sup>, J.D. Hague<sup>3</sup>, J. Hahn<sup>3</sup>, D. Hampf<sup>1</sup>, J. Harris<sup>19</sup>, M. Hauser<sup>20</sup>, S. Heinz<sup>7</sup>, G. Heinzelmann<sup>1</sup>, G. Henri<sup>23</sup>, G. Hermann<sup>3</sup>, A. Hillert<sup>3</sup>, J.A. Hinton<sup>24</sup>, W. Hofmann<sup>3</sup>, P. Hofverberg<sup>3</sup>, M. Holler<sup>7</sup>, D. Horns<sup>1</sup>, A. Jacholkowska<sup>15</sup>, O.C. de Jager<sup>18</sup>, C. Jahn<sup>7</sup>, M. Jamroz<sup>28</sup>, I. Jung<sup>7</sup>, M.A. Kastendieck<sup>1</sup>, K. Katarzyński<sup>29</sup>, U. Katz<sup>7</sup>, S. Kaufmann<sup>20</sup>, D. Keogh<sup>19</sup>, B. Khélifi<sup>11</sup>, D. Klockov<sup>16</sup>, W. Kluźniak<sup>8</sup>, T. Kneiske<sup>1</sup>, Nu. Komin<sup>27</sup>, K. Kosack<sup>9</sup>, R. Kossakowski<sup>27</sup>, F. Krayzel<sup>27</sup>, H. Laffon<sup>11</sup>, G. Lamanna<sup>27</sup>, J.-P. Lenain<sup>20</sup>, D. Lennarz<sup>3</sup>, T. Lohse<sup>13</sup>, A. Lopatin<sup>7</sup>, C.-C. Lu<sup>3</sup>, V. Marandon<sup>3</sup>, A. Marcowith<sup>2</sup>, J. Masbou<sup>27</sup>, N. Maxted<sup>30</sup>, M. Mayer<sup>7</sup>, T.J.L. McComb<sup>19</sup>, M.C. Medina<sup>9</sup>, J. Méhault<sup>2</sup>, R. Moderski<sup>8</sup>, M. Mohamed<sup>20</sup>, E. Moulin<sup>9</sup>, C.L. Naumann<sup>15</sup>, M. Naumann-Godo<sup>9</sup>, M. de Naurois<sup>11</sup>, D. Nedbal<sup>31</sup>, D. Nekrasov<sup>3</sup>, N. Nguyen<sup>1</sup>, B. Nicholas<sup>30</sup>, J. Niemiec<sup>25</sup>, S.J. Nolan<sup>19</sup>, S. Ohm<sup>32,24,3</sup>, E. de Oña Wilhelmi<sup>3</sup>, B. Opitz<sup>1</sup>, M. Ostrowski<sup>28</sup>, I. Oya<sup>13</sup>, M. Panter<sup>3</sup>, M. Paz Arribas<sup>13</sup>, N.W. Pekeur<sup>18</sup>, G. Pelletier<sup>23</sup>, J. Perez<sup>26</sup>, P.-O. Petrucci<sup>23</sup>, B. Peyaud<sup>9</sup>, S. Pita<sup>10</sup>, G. Pühlhofer<sup>16</sup>, M. Punch<sup>10</sup>, A. Quirrenbach<sup>20</sup>, M. Raue<sup>1</sup>, S.M. Rayner<sup>19</sup>, A. Reimer<sup>26</sup>, O. Reimer<sup>26</sup>, M. Renaud<sup>2</sup>, R. de los Reyes<sup>3</sup>, F. Rieger<sup>3,33</sup>, J. Ripken<sup>21</sup>, L. Rob<sup>31</sup>, S. Rosier-Lees<sup>27</sup>, G. Rowell<sup>30</sup>, B. Rudak<sup>8</sup>, C.B. Rulten<sup>19</sup>, V. Sahakian<sup>6,5</sup>, D.A. Sanchez<sup>3</sup>, A. Santangelo<sup>16</sup>, R. Schlickeiser<sup>12</sup>, A. Schulz<sup>7</sup>, U. Schwanke<sup>13</sup>, S. Schwarzbach<sup>16</sup>, S. Schwemmer<sup>20</sup>, F. Sheidaei<sup>10,18</sup>, J.L. Skilton<sup>3</sup>, H. Sol<sup>14</sup>, G. Spengler<sup>13</sup>, Ł. Stawarz<sup>28</sup>, R. Steenkamp<sup>22</sup>, C. Stegmann<sup>7</sup>, F. Stinzing<sup>7</sup>, K. Stycz<sup>7</sup>, I. Sushch<sup>13\*</sup>, A. Szostek<sup>28</sup>, J.-P. Tavernet<sup>15</sup>, R. Terrier<sup>10</sup>, M. Tluczykont<sup>1</sup>, K. Valerius<sup>7</sup>, C. van Eldik<sup>7,3</sup>, G. Vasileiadis<sup>2</sup>, C. Venter<sup>18</sup>, A. Viana<sup>9</sup>, P. Vincent<sup>15</sup>, H.J. Völk<sup>3</sup>, F. Volpe<sup>3</sup>, S. Vorobiov<sup>2</sup>, M. Vorster<sup>18</sup>, S.J. Wagner<sup>20</sup>, M. Ward<sup>19</sup>, R. White<sup>24</sup>, A. Wierzcholska<sup>28</sup>, M. Zacharias<sup>12</sup>, A. Zajczyk<sup>8,2</sup>, A.A. Zdziarski<sup>8</sup>, A. Zech<sup>14</sup>, and H.-S. Zechlin<sup>1</sup>

(Affiliations can be found after the references)

Accepted for publication in A&A

## ABSTRACT

1RXSJ101015.9–311909 is a galaxy located at a redshift of  $z = 0.14$  hosting an active nucleus (called AGN) belonging to the class of bright BL Lac objects. Observations at high (HE,  $E > 100$  MeV) and very high (VHE,  $E > 100$  GeV) energies provide insights into the origin of very energetic particles present in such sources and the radiation processes at work. We report on results from VHE observations performed between 2006 and 2010 with the H.E.S.S. instrument, an array of four imaging atmospheric Cherenkov telescopes. H.E.S.S. data have been analysed with enhanced analysis methods, making the detection of faint sources more significant. VHE emission at a position coincident with 1RXSJ101015.9–311909 is detected with H.E.S.S. for the first time. In a total good-quality livetime of about 49 hours, we measure 263 excess counts, corresponding to a significance of 7.1 standard deviations. The photon spectrum above 0.2 TeV can be described by a power-law with a photon index of  $\Gamma = 3.08 \pm 0.42_{\text{stat}} \pm 0.20_{\text{sys}}$ . The integral flux above 0.2 TeV is about 0.8% of the flux of the Crab nebula and shows no significant variability over the time reported. In addition, public *Fermi*/LAT data are analysed to search for high energy emission from the source. The *Fermi*/LAT HE emission in the 100 MeV to 200 GeV energy range is significant at 8.3 standard deviations in the chosen 25-month dataset. UV and X-ray contemporaneous observations with the *Swift* satellite in May 2007 are also reported, together with optical observations performed with the ATOM telescope located at the H.E.S.S. site. *Swift* observations reveal an absorbed X-ray flux of  $F_{(0.3-7)\text{keV}} = 1.04^{+0.04}_{-0.05} \times 10^{-11} \text{ erg cm}^{-2} \text{ s}^{-1}$  in the 0.3 – 7 keV range. Finally, all the available data are used to study the multi-wavelength properties of the source. The spectral energy distribution (SED) can be reproduced using a simple one-zone Synchrotron Self Compton (SSC) model with emission from a region with a Doppler factor of 30 and a magnetic field between 0.025 and 0.16 G. These parameters are similar to those obtained for other sources of this type.

**Key words.**  $\gamma$ -rays – Galaxies: active – BL Lacertae : individual : 1RXS J101015.9-311909

## 1. Introduction

BL Lac objects are characterised by rapid variability in all energy ranges, and often display jets with apparent superluminal motions. Their extreme properties are thought to be related to the relativistic bulk motion of the emitting region at small angles to the line of sight of the observer. In addition, these objects show highly polarized emission and no or only weak emission lines. The observed broadband Spectral Energy Distribution (SED) of BL Lacs is often comprised of two bumps, one peaking at lower (radio to X-ray), the other peaking at higher (above X-ray) energies. In leptonic scenarios, the lower energy component is generated by synchrotron emission of relativistic electrons moving inside the jet. The higher energy component is due to the inverse Compton scattering of the electrons off the photons of the self-generated synchrotron photon field (SSC models, see for instance Marscher & Gear 1985), or off the photons provided externally by other regions of the source (External Compton or EC models, see for instance Dermer & Schlickeiser 1993). The VHE  $\gamma$ -ray emission in hadronic scenarios can also be explained by the interactions of relativistic protons with ambient photons (Mannheim 1993) or magnetic fields (Aharonian 2000). Depending on the position of the synchrotron component, BL Lacs are subdivided into Low-frequency peaked (LBL) if the maximum of the emission is in the infrared band, and High-frequency peaked (HBL) if the emission is peaked in the UV/X-ray band.

1RXSJ101015.9–311909 belongs to the *ROSAT All Sky Survey Bright Source Catalog* (RASS/BSC) of soft (0.1–2 keV) X-ray sources (Voges et al. 1999), with a flux of  $2.9 \times 10^{-11}$  erg cm $^{-2}$  s $^{-1}$ . It is located at a position of  $(\alpha_{J2000}, \delta_{J2000}) = (10^{\text{h}}10^{\text{m}}15.9^{\text{s}}, -31^{\circ}19'09'')^1$  and has a redshift of  $z = 0.14$  (see Piranomonte et al. 2007 for both measurements). The source is present in the NRAO VLA Sky Survey (NVSS) catalogue of radio sources at 1.4 GHz (Condon et al. 1998), which lists its flux density as  $73.5 \pm 2.7$  mJy. A radio flux of  $89.5 \pm 3.6$  mJy in the 843 MHz band has been measured by the SUMSS radio survey (Bock et al. 2011). Due to its extreme value of the X-ray to radio flux ratio and its high X-ray flux, 1RXSJ101015.9–311909 passed the criteria for inclusion in the Sedentary Multi-Frequency Survey catalogue (Giommi et al. 2005). This catalogue specifically selected HBLs and thus presented an obvious choice for the extension of the list of VHE BL Lac candidates. 1RXSJ101015.9–311909 also fulfilled the criteria proposed in Costamante & Ghisellini (2002), where BL Lac candidates are considered interesting targets if they exhibit high levels of both X-ray and radio emission.

Following these indications, observations of this source with H.E.S.S. started at the end of 2006, yielding the discovery of  $\gamma$ -ray emission from 1RXSJ101015.9–311909 (see Sec. 2) reported here. By combining this information with other multi-wavelength data, the properties of the detected emission and its physical implications are discussed. The HE emission of the source has been studied with *Fermi*/LAT public data between 100 MeV and 200 GeV and results are reported here in Sec. 3.1. Analysis of data at lower energy bands is carried out to understand the emission from this source: *Swift* data (from the XRT

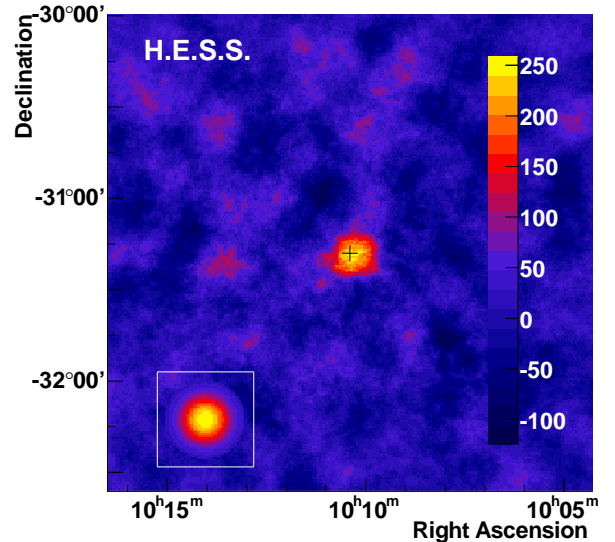


**Fig. 1.** Image of 1RXSJ101015.9–311909 in right ascension and declination (J2000) of the  $\gamma$ -ray excess found by H.E.S.S. oversampled with the 68% containment radius of the point spread function ( $0.11^\circ$  for these analysis cuts). The cross represents the nominal position of the source. The inset on the lower left shows the expected  $\gamma$ -ray excess distribution from a point-like source.

and UVOT telescopes) are analysed and discussed in Sec. 3.2 and 3.3, and optical data from the ATOM (Automatic Telescope for Optical Monitoring, Hauser et al. 2004) telescope located on the H.E.S.S. site and taken mostly contemporaneously to the H.E.S.S. data, are analysed and discussed in Sec. 3.4. Finally, in Sec. 4 all the available data are used to study the global SED of the source in the context of a simple SSC scenario.

## 2. H.E.S.S. observations and results

H.E.S.S. is an array of four imaging Cherenkov telescopes located in the southern hemisphere in the Khomas Highland of Namibia (Aharonian et al. 2006), that detects cosmic  $\gamma$ -rays in the 100 GeV to 100 TeV energy range. Each of the telescopes is equipped with a segmented mirror of 107 m $^2$  area and a camera composed of 960 photomultipliers covering a large field-of-view (FoV) of  $5^\circ$  diameter. The stereoscopic system works in a coincidence mode, requiring at least two of the four telescopes to trigger the detection of an extended air shower. The trigger threshold, defined as the peak of the differential  $\gamma$ -ray rate for a Crab-like source at Zenith (Funk et al. 2004), is about 100 GeV and increases with increasing zenith angle.

Observations of 1RXSJ101015.9–311909 were carried out with H.E.S.S. in a campaign of 64 hours of observation time between 2006 and 2010. These cover a range of zenith angles between  $8^\circ$  and  $28^\circ$ , giving an average zenith angle of  $12.9^\circ$ , with a pointing offset of  $0.5^\circ$  relative to the nominal position of the source (see Tab. 1 for all details). The data from a total high-quality livetime of  $\sim 48.7$  hours (after hardware and weather quality selection criteria were applied with a procedure similar to that described in Aharonian et al. 2006) have been analysed to search for emission at the nominal position of the source.

The analysis of the  $\gtrsim 100$  GeV  $\gamma$ -ray emission from this AGN is carried out with the analysis procedure described in

Send offprint requests to:

Yvonne Becherini - Yvonne.Becherini@apc.univ-paris7.fr

Matteo Cerruti - Matteo.Cerruti@obspm.fr,

Jean-Philippe Lenain - jean-philippe.lenain@lsw.uni-heidelberg.de

\* supported by Erasmus Mundus, External Cooperation Window

<sup>1</sup> This is the position from the RASS/BSC. It will be later referred to as the *nominal position* of the source.

**Table 1.** Summary of good-quality data of H.E.S.S. observations of 1RXS J101015.9–311909 over the years 2006 – 2010.

year	MJD (start)	MJD (end)	$N_{\text{runs}}$	LT	zen	$N_{\text{ON}}$	$N_{\text{OFF}}$	$N_{\gamma}$	$\sigma$
2006	54090.09	54090.11	1	0.43	12.7	17	126	5.5	1.5
2007	54142.95	54238.79	35	14.52	11.7	551	4835	111.5	4.9
2008	54475.07	54535.92	12	5.37	10.1	136	1291	18.6	1.6
2009	54832.06	54976.79	36	15.62	14.4	457	3968	96.2	4.6
2010	55265.90	55299.84	29	12.80	13.6	255	2466	30.8	1.9
Tot.	54090.09	55299.84	113	48.70	12.9	1416	12686	262.7	7.1

**Notes.** The columns represent the year in which the source has been observed, the start and end date of observations in MJD, the number of good-quality runs available  $N_{\text{runs}}$ , the corresponding exposure time in hours (LT), the mean observation zenith angle  $\text{zen}$  in degrees, the number of ON- ( $N_{\text{ON}}$ ) and OFF-source ( $N_{\text{OFF}}$ ) events, the number of excess events  $N_{\gamma}$  and the significance of the detection in units of standard deviations  $\sigma$ . The observation offset and the background normalization factor  $\alpha$  (see text) for all datasets presented in the table are  $0.5^\circ$  and 0.09, respectively.

Becherini et al. (2011), where an enhanced low-energy sensitivity with respect to standard analysis methods (Aharonian et al. 2006) is achieved. This new analysis method is based on a multivariate signal-to-background discrimination procedure using both previously-known and newly-derived discriminant variables which depend on the physical shower properties, as well as its multiple images. In order to have a lower threshold for this source, the analysis configuration with a charge value of 40 photoelectrons has been used as a minimal required total amplitude for the cleaned and parametrized image in each telescope.

The VHE  $\gamma$ -ray emission from the BL Lac object 1RXS J101015.9–311909 is detected using the *Reflected* background modelling method (Aharonian et al. 2006) with a statistical significance<sup>2</sup> of 7.1 standard deviations. The significance of the detection is represented by an excess of 263 counts at the nominal position of the source, the total number of ON- and OFF-source events being  $N_{\text{ON}} = 1416$  and  $N_{\text{OFF}} = 12686$ , respectively, with a background normalization factor<sup>3</sup>  $\alpha = 0.09$ .

The VHE  $\gamma$ -ray excess image obtained with the *Ring* background modelling method (Aharonian et al. 2006) is shown in Fig. 1, while Fig. 2 shows the ON-source and normalized OFF-source angular distributions ( $\theta^2$ ) for all H.E.S.S. observations: the background is rather flat, as expected at very small  $\theta^2$ , and there is a clear excess at small values of  $\theta^2$ , corresponding to the observed signal. A fit to the excess events of a point-like source model convolved with the H.E.S.S. point-spread-function (PSF) yields a position  $\alpha_{\text{J2000}} = 10^{\text{h}}10^{\text{m}}15.03^{\text{s}} \pm 3.77^{\text{s}}_{\text{stat}} \pm 1.56^{\text{s}}_{\text{sys}}$  and  $\delta_{\text{J2000}} = -31^\circ18'18.4'' \pm 41.6''_{\text{stat}} \pm 20''_{\text{sys}}$ , consistent with the position of the radio and X-ray source (see Fig. 3). The  $3\sigma$  upper limit to the intrinsic source extension calculated at the best fit position is  $3.4'$ .

The time-averaged differential VHE  $\gamma$ -ray spectrum of the source, derived using the forward-folding technique described in Piron et al. (2001), is presented in Fig. 4. The spectrum is well fitted by a power-law function  $dN/dE = \phi_0 \times (E/1 \text{ TeV})^{-\Gamma}$  with a normalization of  $\phi_0 = (1.87 \pm 0.66_{\text{stat}} \pm 0.37_{\text{sys}}) \times 10^{-13} \text{ cm}^{-2} \text{ s}^{-1} \text{ TeV}^{-1}$  and photon index  $\Gamma = 3.08 \pm 0.42_{\text{stat}} \pm 0.20_{\text{sys}}$ . The differential flux at the decorrelation energy ( $E_{\text{dec}} = 0.51 \text{ TeV}$ ) is  $\phi_{E_{\text{dec}}} = (1.47 \pm 0.31_{\text{stat}} \pm 0.29_{\text{sys}}) \times 10^{-12} \text{ cm}^{-2} \text{ s}^{-1} \text{ TeV}^{-1}$ . The integral flux above the analysis threshold<sup>4</sup>  $E_{\text{th}} = 0.2 \text{ TeV}$  is  $\phi(E > E_{\text{th}}) = (2.35 \pm 0.64_{\text{stat}} \pm 0.47_{\text{sys}}) \times$

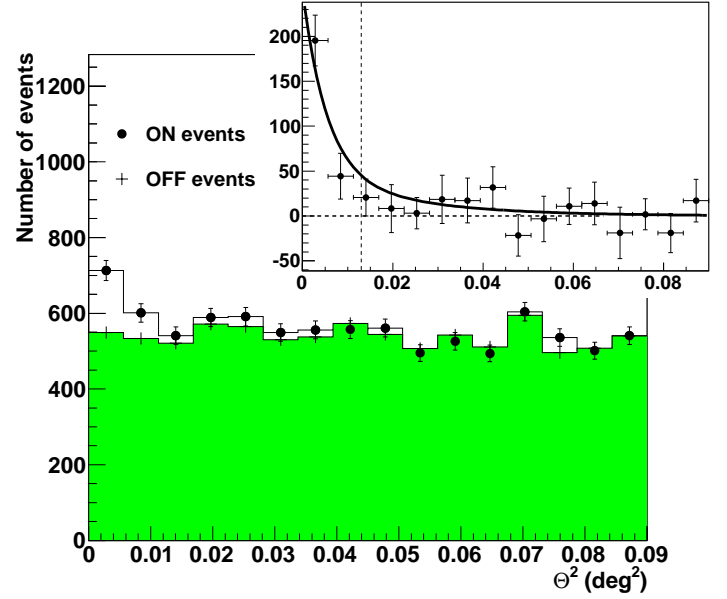


**Fig. 2.** The distribution of  $\theta^2$  for ON-source events and normalized OFF-source events centered at the nominal position from H.E.S.S. observations of 1RXS J101015.9–311909. In the inset:  $\theta^2$  distribution of the excess at the fitted position of the AGN; the superposed line is a fit of the PSF to the data. The containment radius at 68% of the PSF for the given observation conditions is  $0.116^\circ$  and is shown by the dashed vertical line.

$10^{-12} \text{ cm}^{-2} \text{ s}^{-1}$ , corresponding to  $\sim 0.8\%$  of the flux of the Crab nebula above the same threshold. No significant variability is detected; the integral flux is seen to be constant within errors over the H.E.S.S. dataset, as shown in Fig. 5. A fit of the period-by-period<sup>5</sup> light curve with a constant value yields a  $\chi^2/\text{dof} = 11.39/9$ , with a probability of 25%. The measured normalized excess variance of  $0.44 \pm 0.71$  on the same light curve yields a 99% confidence level upper limit on the fractional variance<sup>6</sup> of  $\leq 151\%$ , as calculated using the method of Feldman & Cousins (1998). No variability can be seen either in other time binnings tested (year-by-year or run-by-run). All analysis results have been cross-checked and confirmed with an independent method (de Naurois & Rolland 2009), which gives consistent results.

<sup>5</sup> A H.E.S.S. observing period is the period between two full moons.

<sup>6</sup> See Vaughan et al. (2003) for definitions of normalized and fractional excess variance.

<sup>2</sup> Calculated following Eq. (17) of Li & Ma (1983).

<sup>3</sup> In the *Reflected* background method  $\alpha$  is just the reciprocal of the number of OFF-source regions considered.

<sup>4</sup> For this analysis the threshold energy is defined as the energy at which the effective detection surface exceeds two hectares and where the energy bias is less than twice the energy resolution.

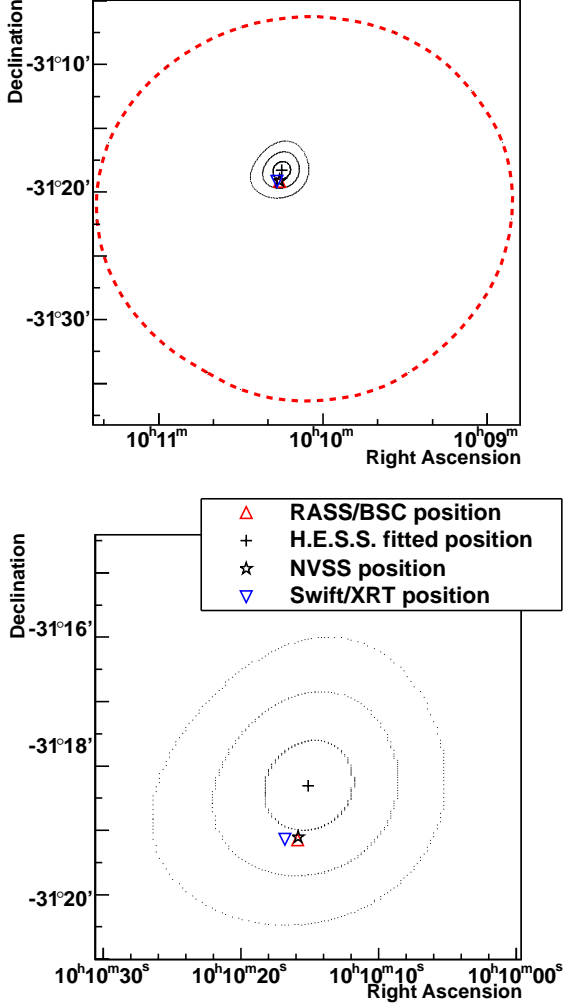


**Fig. 3.** *Upper panel.* The three contour lines around the H.E.S.S. fitted position of 1RXS J101015.9–311909 correspond to the error contours at 1, 2 and 3 standard deviations on the position evaluation. The red dashed line represents the  $1\sigma$  significance contour of the *Fermi*/LAT detection of the source. *Bottom panel.* Zoom on the H.E.S.S. fitted position, represented by the cross and the error contours, compared to the X-ray (*Swift*/XRT and ROSAT) and radio (NVSS) positions.

### 3. Multi-wavelength observations

#### 3.1. Analysis of *Fermi*/LAT data

1RXS J101015.9–311909 has been associated with the object 2FGL J1009.7–3123 in the *Fermi*/LAT second source catalogue (Abdo et al. 2011). A *Fermi*/LAT data analysis is performed on the publicly available data, spanning the time interval from 2008-08-04 (MJD 54682) to 2011-01-01 (MJD 55562), using the binned likelihood method (Atwood et al. 2009) from the *Science Tools* package V. v9r23p1, following the procedure recommended by the *Fermi*/LAT collaboration<sup>7</sup>.

The isotropic model `iso.p7v6source` is used to account for both the extragalactic diffuse emission and residual instrumental background, while the spatial template `gal_2yearp7v6.v0` is

**Table 2.** Spectral properties for the analysis of *Fermi*/LAT data.

$E_{\text{th}}$	$\Gamma$	TS	$\phi(E > E_{\text{th}})$	$E_{\text{dec}}$
100	$2.09 \pm 0.15_{\text{stat}}$	68.29	$11.31 \pm 3.83_{\text{stat}}$	1929
300	$1.92 \pm 0.15_{\text{stat}}$	62.73	$2.54 \pm 0.69_{\text{stat}}$	3259
500	$1.82 \pm 0.15_{\text{stat}}$	59.82	$1.36 \pm 0.34_{\text{stat}}$	4306
1000	$1.71 \pm 0.16_{\text{stat}}$	55.93	$0.70 \pm 0.16_{\text{stat}}$	5863

**Notes.** The columns correspond to the energy threshold in MeV,  $E_{\text{th}}$ , the photon index,  $\Gamma$ , the test statistic (TS), the integral flux above threshold  $\phi(E > E_{\text{th}})$  in units of  $10^{-9} \text{ ph cm}^2 \text{ s}^{-1}$  and the decorrelation energy ( $E_{\text{dec}}$ ) in MeV. The *Fermi*/LAT systematic uncertainty on the spectral index is 10% at 100 MeV, decreasing to 5% at 560 MeV and increasing to 10% at 10 GeV and above, see Abdo et al. (2011).

used to account for the contribution from the Galactic diffuse emission.

Since 1RXS J101015.9–311909 lies at a Galactic latitude of  $20.05^\circ$ , the centre of the region of interest (RoI) is taken  $5^\circ$  away in the North-East direction from its nominal position in order to minimize the contribution from the Galactic diffuse emission.

In the analysis presented here, source-class events are considered in a circular RoI of  $10^\circ$  radius, and the P7V6\_SOURCE instrumental response functions were used. In order to account for the potential contamination of events from sources outside the RoI due to the large PSF at low energies, all the neighbouring 2FGL objects are included in the model reconstruction of the source up to a radius of  $15^\circ$ .

Using the *glike* tool and assuming a power-law shape for the source spectrum, the Test Statistic (TS, Mattox et al. 1996) of the binned likelihood analysis is 68.3, corresponding approximately to a  $8.3\sigma$  detection in the 100 MeV – 200 GeV energy range. The corresponding photon index is  $\Gamma = 2.09 \pm 0.15_{\text{stat}}$  and the highest energy photon from the direction of the source (i.e., within the 95% containment radius of the PSF at the given energy) has an energy of 76.6 GeV. Other, more complex spectral shapes like a log-parabola or a broken power-law do not result in a significant improvement of the fit, and thus the power-law spectral shape is used in the remainder of this paper. The resulting spectral slope under these assumptions is consistent with the value found in the 2FGL catalogue, which gives  $\Gamma = 2.24 \pm 0.14_{\text{stat}}$ .

However, there is evidence for a dependence of the photon index on the chosen energy threshold in the data analysis as summarized in Tab. 2. The spectrum of the source tends to harden with an increasing low-energy cut, which could be an indication of a curved spectrum. Future observations with *Fermi*/LAT may enable a significant detection of a possible curvature of the spectrum compared to a pure power-law.

To further check these results, a test was performed by modelling the Galactic diffuse emission with a power-law spectrum, instead of using a constant flux normalisation for this component, as is usually recommended by the *Fermi*/LAT team. Such an energy-dependent spectrum for this component would be an indication for a mis-modelled Galactic diffuse emission in the analysis, and could affect the hardening tendency as a function of the energy threshold reported in Tab. 2. When using a threshold of 100 MeV, the latter test results in a photon index of  $\Gamma = 0.07 \pm 0.01$  for the Galactic diffuse component, while the spectral results for the AGN remain fully compatible with those reported in Tab. 2. This slight energy-dependence of the spectrum of the Galactic model just reflects the fact that the mechanism responsible for the HE emission from the Galaxy is not yet perfectly understood, but does not strongly affect our re-

<sup>7</sup> see <http://fermi.gsfc.nasa.gov/ssc/data/analysis>.



sults. While at each of the energy thresholds the count map of the RoI exhibits a visible gradient due to the Galactic diffuse emission, no such gradient is present in the residual map after subtraction of the Galactic and extragalactic models and the 2FGL sources (including 1RXS J101015.9–311909), being rather flat within the counting error. This shows that the normalization of the Galactic diffuse emission is under control and well-modelled in this analysis.

In the following, we will adopt the results of *Fermi*/LAT data analysis using the two energy thresholds of 300 MeV and 1 GeV, see Fig. 4.

The choice of a 300 MeV threshold is made in order to minimize a possible contamination at low energies from neighbouring sources and from the Galactic diffuse emission. This choice takes into account the tendency of the spectrum to harden with increasing energy threshold, while not losing too many source photons due to this cut. We choose 1 GeV as a second threshold in order to study how the evaluation of the *Fermi*/LAT slope affects the modelling of the overall SED (see Fig. 7).

The *Fermi*/LAT binned spectral points shown in Fig. 7 are computed by running *gtlike* in five contiguous energy bins, using the model parameters from the likelihood fit on the energy range 1 GeV – 200 GeV, where the spectral index of 1RXS J101015.9–311909 was fixed to the best value of  $\Gamma = 1.71$  (see Tab. 2). An upper limit on the flux in a given energy bin was computed if  $TS < 9$ . The resulting fluxes for all analyses can be found in Tab. 2.

The *Fermi*/LAT light curves, for the two chosen threshold energies, are shown in Fig. 5, where the data are presented in a 6-month binning: given the low photon statistics, no significant variability is found in the 25 months of data. This was checked using other time binnings ranging from 90 to 180 days.

The *Fermi*/LAT position of 1RXS J101015.9–311909 has been optimized using the tool *gtfindsrc*, and the best fit was found to be at the position  $(\alpha_{J2000}, \delta_{J2000}) = (10^h09^m49.51^s, -31^\circ24'21.9'')$  which is fully consistent with the position reported in the 2FGL catalogue ( $\sim 3'$  away). The  $1\sigma$  contour presented in Fig. 3 was derived from the TS map computed on the RoI, using the best-fit position of the source.

### 3.2. *Swift*/XRT

The X-ray Telescope (XRT) (Burrows et al. 2005) on board the  $\gamma$ -ray burst mission *Swift* (Gehrels et al. 2004) observed 1RXS J101015.9–311909 three times during 2007-05-17 and 2007-05-18 (see Tab. 3 for the total exposure time available with *Swift*/XRT). The first and third observations were performed in photon-counting (*pc*) mode, while the second observation was performed in windowed-timing (*wt*) mode. Cleaned event files have been reduced using *HEASoft*<sup>8</sup>, V. 6.7. Source spectra and lightcurves have been extracted using *XSelect*, V. 2.4a, and the spectral fitting has been performed using *XSpec*, V. 12.5.1. Response matrices and ancillary response files have been provided by the *Swift*/XRT instrument team. The source count-rate is equal to  $0.4 \text{ counts s}^{-1}$  for the three observations. The presence of a pile-up effect in the data has been checked following the prescriptions of the *Swift*/XRT instrument team<sup>9</sup>, leading to the conclusion that it does not affect the observations. As no significant variability has been observed, the two spectra obtained in the *pc*-mode have been summed using *mathpha*, V. 4.1.0, and fitted together with the second observation spectrum. Data

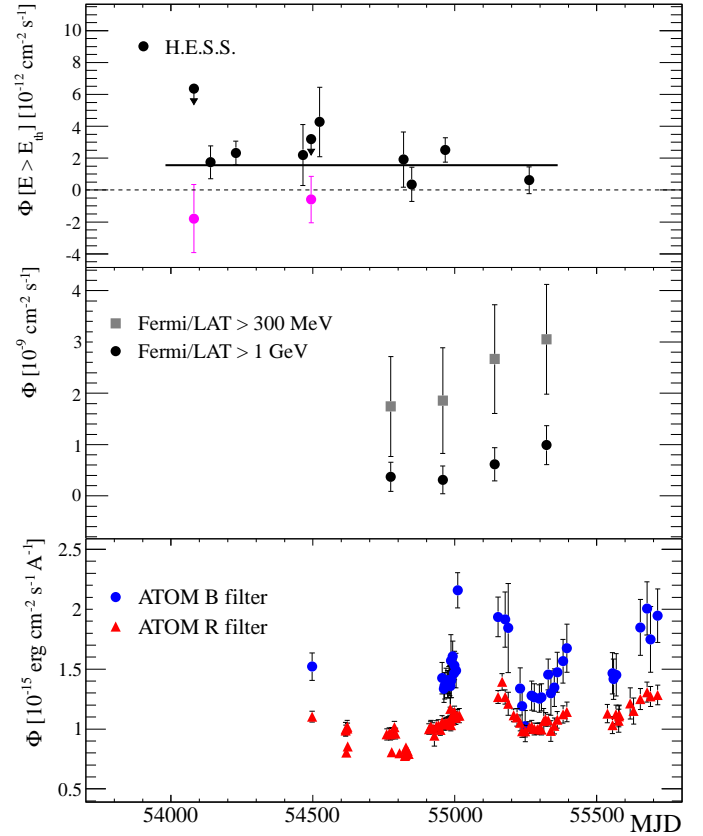


**Fig. 5.** *Upper panel.* Light curve of H.E.S.S. observations. The mean flux above 0.2 TeV per observing period (between two full moons) is shown as a function of the time in MJD. Only statistical errors are shown. Upper limits at 99% confidence level are calculated when no signal is found and in this case the corresponding negative fluxes are shown in magenta. The solid line represents the fit of a constant to the H.E.S.S. data. *Middle panel.* Light curves of *Fermi*/LAT observations for the  $E_{th} > 300$  MeV and  $E_{th} > 1$  GeV thresholds in a 6-month binning. The first two flux points of the  $E_{th} > 300$  MeV light curve and the first three flux points of the  $E_{th} > 1$  GeV light curve have a  $TS < 9$ . *Bottom panel.* Light curve of ATOM observations with R and B filters, corrected for Galactic extinction assuming  $E_{B-V} = 0.104$  (case A).

below 0.3 keV have not been included in the analysis<sup>10</sup> while the last significant bin is at  $\approx 7$  keV. The spectra have been rebinned using *grppha*, V. 3.0.1, in order to have a minimum of 10 counts per bin. The Galactic column density  $N_H$  has been fixed at  $7.79 \times 10^{20} \text{ cm}^{-2}$ , as evaluated by Dickey & Lockman (1990).

A fit performed using a simple power-law function with Galactic absorption gives  $\Gamma = 2.15 \pm 0.06$  and normalization factor  $C_{1 \text{ keV}} = (3.0 \pm 0.1) \times 10^{-3} \text{ keV}^{-1} \text{ cm}^{-2} \text{ s}^{-1}$  ( $\chi^2/\text{dof} = 172/141$ ). The fit is significantly improved (F-test probability equal to  $4 \times 10^{-6}$ ) if a broken power-law is assumed, as shown in Tab. 4, case A, where the best fit parameters for the two photon indices, break energy and normalization are presented. The absorbed flux in the 0.3 – 7 keV energy band is found to be  $(1.04^{+0.04}_{-0.05}) \times 10^{-11} \text{ erg cm}^{-2} \text{ s}^{-1}$ .

<sup>8</sup> <http://heasarc.nasa.gov>

<sup>9</sup> <http://www.swift.ac.uk/pileupthread.shtml>

<sup>10</sup> [http://heasarc.gsfc.nasa.gov/docs/heasarc/caldb/swift/docs/xrt/SWIFT-XRT-CALDB-09\\_v16.pdf](http://heasarc.gsfc.nasa.gov/docs/heasarc/caldb/swift/docs/xrt/SWIFT-XRT-CALDB-09_v16.pdf)

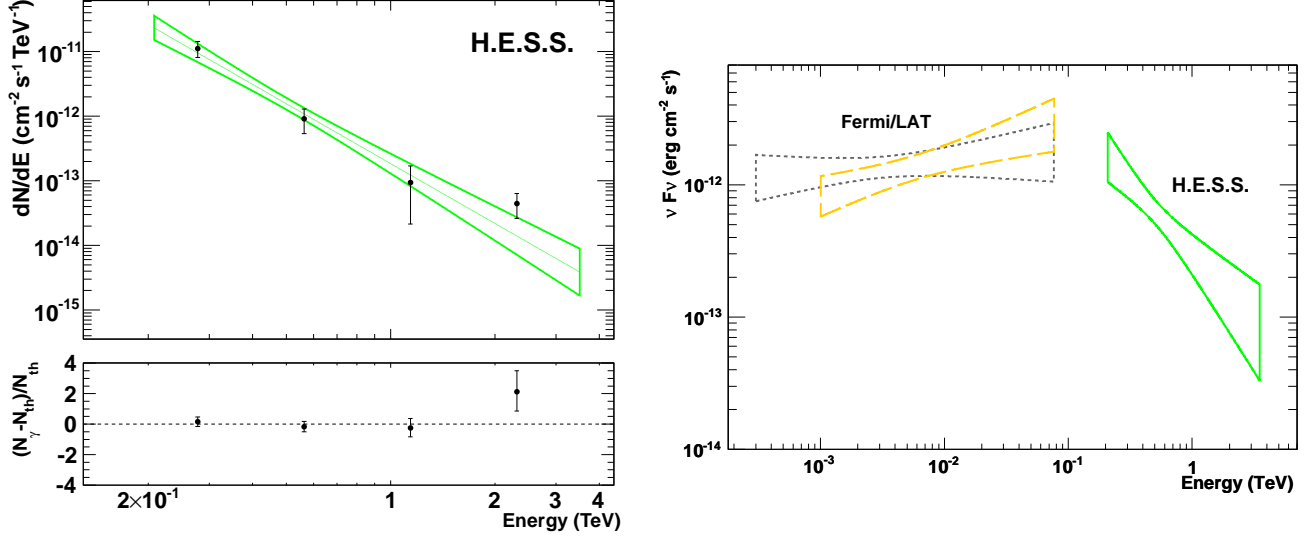


**Fig. 4.** *Left panel.* Time-averaged VHE spectrum measured from the direction of 1RXS J101015.9–311909. The bow-tie represents  $1\sigma$  confidence level error band of the fitted spectrum using a power-law hypothesis. The lower panel shows the fit residuals, i.e.  $(N_\gamma - N_{\text{theo}})/N_{\text{theo}}$ , where  $N_\gamma$  and  $N_{\text{theo}}$  are the detected and expected number of excess events, respectively. *Right panel.* *Fermi/LAT* and H.E.S.S. bow-ties. The two *Fermi/LAT* bow-ties represent the  $E_{\text{th}} > 300$  MeV (dotted line) and the  $E_{\text{th}} > 1$  GeV (dashed line) spectral results. All the bow-ties (H.E.S.S. and *Fermi/LAT*) result from a forward-folding spectral analysis technique.

**Table 3.** *Swift* observations available for 1RXS J101015.9–311909.

	ID	Mode	Start	Exposure (s)
obs. 1	00030940002	pc	2007-05-17	1744
obs. 2	00030940003	wt	2007-05-18	790
obs. 3	00030940004	pc	2007-05-18	1981
tot				4515

**Notes.** In the photon-counting (pc) mode the entire charge-coupled device is read out, while in the windowed-timing (wt) mode only the central rows of the camera are read, increasing the time resolution of the instrument.

**Table 4.** Parameters of the two hypotheses under consideration for the fit of the *Swift*/XRT data.

Case	$\Gamma$	$E_{\text{break}}$ [keV]	$C_{1\text{keV}}$	$N_{\text{H,free}}$	$\chi^2/\text{d.o.f.}$
A	$\Gamma_1 = 1.8^{+0.2}_{-0.2}$ $\Gamma_2 = 2.5^{+0.3}_{-0.2}$	$1.4^{+0.5}_{-0.2}$	$3.2^{+0.2}_{-0.2}$		144/139
B	$\Gamma = 2.5^{+0.1}_{-0.1}$		$3.9^{+0.4}_{-0.4}$	$9^{+4}_{-3}$	147/140

**Notes.**  $\Gamma$  is the fitted photon index, and  $E_{\text{break}}$  is the energy at which the break in the spectrum occurs. Case A represents the broken power-law hypothesis considering only the absorption in the Galaxy, while case B represents the power-law fit taking into account the absorption in the Galaxy plus a second absorber ( $N_{\text{H,free}}$ , expressed in units of  $10^{20} \text{ cm}^{-2}$ ) located at the redshift of the source. The normalization  $C_{1\text{keV}}$  is given in units of  $10^{-3} \text{ keV}^{-1} \text{ cm}^{-2} \text{ s}^{-1}$ .

The break observed in the X-ray spectrum (see Fig. 6) can either be intrinsic or external, i.e. due to an additional absorption component in the AGN host galaxy. For an extensive discussion about this topic see Perlman et al. (2005), where based on the analysis of XMM-Newton spectra of 13 different BL Lac objects, a discussion of the intrinsic or external origin of the ob-

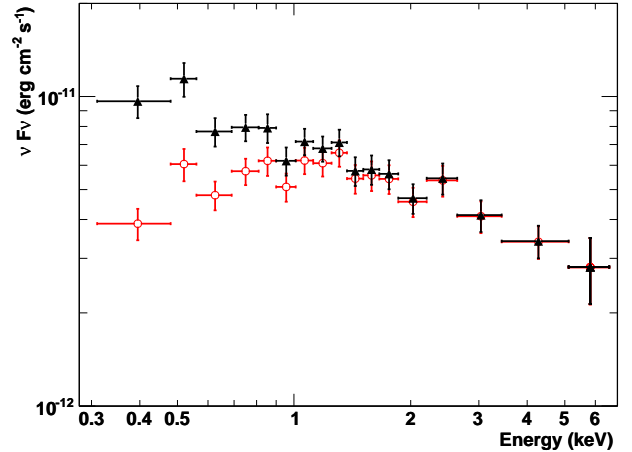


**Fig. 6.** The two *Swift*/XRT spectra for case A (galactic absorption only) and B (additional absorption), corrected for the respective absorptions, are shown in this figure by the red points and the black triangles, respectively. For simplicity, only the spectrum from the pc-mode observations, rebinned for plotting purposes, is presented.

served spectral curvature is given, concluding that the first hypothesis would be preferred. The hypothesis of an external origin of the break has been tested by fitting the *Swift*/XRT data with a power-law emission function including absorption by Galactic material (fixed at the value given by Dickey & Lockman 1990) plus a second absorber located at the redshift of the host galaxy with adjustable column density. The best fit in this case (case B in Tab. 4) is statistically equivalent to the broken power-law, the evaluation of the second absorber column density being

$N_{\text{H,free}} = 9^{+4}_{-3} \times 10^{20} \text{ cm}^{-2}$ . This second absorber is, however, poorly constrained compared to the Galactic one.

It should be noted that, given the relatively low redshift of the source, the location of the absorber cannot be constrained. In particular, the same absorption effect could be obtained by multiplying by a factor of  $\sim 2$  the contribution of the Galactic absorption in the direction of the source. However, such a high value of the Galactic column density is not consistent with the range of  $N_{\text{H}}$  measured in a circle of  $1^\circ$  around the nominal position of the source (Dickey & Lockman 1990).

The deabsorbed X-ray spectra of the source assuming either an intrinsic break of the spectrum (corrected only for Galactic absorption), or an external one (corrected for both absorbers), are shown in Fig. 6.

### 3.3. *Swift*/UVOT

The *Swift* satellite carries an Ultra-Violet/Optical Telescope (UVOT) (Romig et al. 2005), which observed 1RXS J101015.9–311909 simultaneously with XRT. Six different filters are available: V and B in optical and U, UVW1, UVM2 and UVW2, in the ultra-violet, in order of increasing frequency. Counts have been extracted in a  $5''$  radius of aperture, and magnitudes and fluxes have been evaluated using *uvotmaghist*, V. 1.1. The correction for Galactic extinction has been done following Roming et al. (2009), assuming  $E_{B-V} = 0.104$  and  $0.224$  for case A and B respectively, where  $E_{B-V}$  is the difference of the total extinction in the B and V filters. The evaluation of  $E_{B-V}$  has been done using  $N_{\text{H}} = 7.79$  and  $16.79 \times 10^{20} \text{ cm}^{-2}$ , for case A and B, respectively, and  $N_{\text{H}}/E_{B-V} = 7.5 \times 10^{21} \text{ cm}^{-2}$ , as given in Jenkins & Savage (1974). No significant variability in the data is observed. Therefore, the mean flux values measured by UVOT for each filter are used for the study of the SED (see Sec. 4).

### 3.4. ATOM

ATOM (Hauser et al. 2004) is a 75-cm optical telescope located at the H.E.S.S. site. 1RXS J101015.9–311909 has been regularly observed with ATOM from January 2008 to June 2011. On 2008-02-01 the source has been observed with B, R and I filters (as defined by Bessell 1990) while the rest of the observations have been performed in the B and R bands, only. The fluxes have been determined using a  $4''$  radius of aperture. The evaluation of the errors includes the uncertainty of the absolute calibration. As shown in the lower panel of Fig. 5, the source varies significantly in both the B ( $79\% \pm 11\%$ , evaluated as the difference between the highest and the lowest flux measured over the mean value) and R ( $62\% \pm 8\%$ ) energy bands. The measured normalized excess variances of  $(0.014 \pm 0.005)_B$  and  $(0.011 \pm 0.002)_R$  confirm that there is a significant variability in both the blue and red bands, respectively. The lowest detected variability time-scale is roughly 1 day, corresponding to the minimum time between two different observations. The measured I band spectral flux density, not shown in Fig. 5, is  $(7.84 \pm 0.33) \times 10^{-16} \text{ erg cm}^{-2} \text{ s}^{-1} \text{ \AA}^{-1}$ . For the SED (Sec. 4), the mean flux obtained from ATOM data, corrected for Galactic extinction (again using  $E_{B-V} = 0.104$  and  $0.224$  for case A and B, respectively), is considered; the error bars show the flux variability range observed.

**Table 5.** Parameters used for the SSC modelling of the SED of 1RXS J101015.9–311909 and derived physical quantities.

	Fermi- $>300 \text{ MeV}$		Fermi- $>1 \text{ GeV}$	
	Case A	Case B	Case A	Case B
$\gamma_{e,\text{break}}$	$1.08 \times 10^5$	$9.0 \times 10^4$	$1.01 \times 10^5$	$7.8 \times 10^4$
$\alpha_1$	2.2	2.2	2.0	2.0
$K$	$5.67 \times 10^4$	$3.37 \times 10^2$	$6.6 \times 10^3$	$4.5 \times 10^1$
$u_e$	$5.37 \times 10^{-2}$	$3.15 \times 10^{-4}$	$3.42 \times 10^{-2}$	$2.24 \times 10^{-4}$
B	0.16	0.025	0.16	0.025
$u_B$	$1.02 \times 10^{-3}$	$2.49 \times 10^{-5}$	$1.02 \times 10^{-3}$	$2.49 \times 10^{-5}$
$u_e/u_B$	52.7	12.7	33.6	9.0
R	$2.37 \times 10^{15}$	$7 \times 10^{16}$	$2.37 \times 10^{15}$	$7 \times 10^{16}$
$\tau_{\text{var}}$	0.8	24.7	0.8	24.7
$L_{\text{jet}}$	$7.6 \times 10^{42}$	$4.1 \times 10^{43}$	$4.9 \times 10^{42}$	$3.0 \times 10^{43}$

**Notes.** Summary of the SED parameters for the two *Fermi*/LAT spectra considered (low-energy threshold equal to 300 MeV and 1 GeV) and for the two cases proposed in the *Swift*/XRT analysis (case A and case B). For all the cases considered, the minimum and maximum Lorentz factors of the electron distribution are set to  $\gamma_{e,\text{min}} = 300$  and  $\gamma_{e,\text{max}} = 5 \times 10^6$  respectively; the angle to the line of sight is  $\theta = 1^\circ$ , the Doppler factor is  $\delta = 30$ , and the index of the electron distribution after the break is  $\alpha_2 = 4.0$ . The electron-distribution normalization parameter  $K$  is in units of  $\text{cm}^{-3}$ ; the magnetic field  $B$  is in G; the emitting-region size  $R$  is in cm; the energy densities  $u_{e,B}$  are in  $\text{erg cm}^{-3}$ ; the variability timescale  $\tau_{\text{var}}$  is in hours and the jet luminosity  $L_{\text{jet}}$  is in  $\text{ergs s}^{-1}$ .

## 4. SSC modelling of the SED

The non-simultaneous SED of 1RXS J101015.9–311909, corrected for Galactic absorption, is shown in Fig. 7. Historical data taken from NED<sup>11</sup> are also shown. Before 2006 the source has been observed in radio, infrared, optical and X-rays. A discussion of the accuracy of the cross-calibration between *Fermi*/LAT and H.E.S.S. (evaluated at 4% based on the Crab nebula) can be found in Meyer et al. (2010).

The optical flux contribution from the host galaxy has been evaluated using data from the 2MASS Extended Source catalogue (Jarrett et al. 2000). Based on the magnitude values evaluated for different radii of aperture ( $r > 5''$ ) and the effective radius of the galaxy ( $r_{\text{eff}} = 3.03''$  in the J band), we estimate this contribution in a  $4''$  radius of aperture as  $m_{\text{gal}} \simeq 14.3$  for the magnitude in the J band, following Young (1976). The magnitude obtained has been used to properly rescale the template of a giant elliptical galaxy spectrum (evaluated using PEGASE) (Fioc & Rocca-Volmerange 1997).

As shown in Fig. 7, in infrared light, the host galaxy dominates the AGN emission. This is consistent with the optical spectrum measured by Piranomonte et al. (2007) when evaluating the redshift of the source (see Fig. 2 and A. 1 in their paper) and with the fact that the variability amplitude in the B band is significantly larger than that in the R band.

The emission from the active nucleus is described using a stationary one-zone SSC code (Katarzyński et al. 2001): a spherical plasma blob (characterised by its radius  $R$ ) moving with Doppler factor  $\delta$  in the relativistic jet (with  $\theta$  being the angle to the line of sight) is filled with a homogeneous magnetic field  $B$  and a stationary, non-thermal electron distribution. The synchrotron emission from these electrons is responsible for the low energy bump, peaking in the X-ray band, and is then Compton-upscattered by the electrons themselves, to produce the  $\gamma$ -ray

<sup>11</sup> NASA/IPAC extragalactic database, <http://ned.ipac.caltech.edu>.

emission. Pair production ( $\gamma + \gamma \rightarrow e^- + e^+$ ) inside the blob is not negligible, and is taken into account using the cross section evaluated by Aharonian et al. (2008). The interaction between VHE photons escaping the source and the infrared extragalactic background light (EBL) produces  $e^+e^-$  pairs as well, and induces an absorption in the observed VHE spectrum of the source. This effect has been taken into account using the EBL model from Franceschini et al. (2008), which is compatible with the EBL limit inferred from VHE observations (Aharonian et al. 2006a). The primary electron distribution ( $N(\gamma_e)$ , where  $\gamma_e$  is the Lorentz factor of the electrons), defined between  $\gamma_{e,\min}$  and  $\gamma_{e,\max}$ , is modeled using a broken power-law function<sup>12</sup> with normalization  $K$  (defined as the number density of electrons at  $\gamma_e = 1$ , in units of  $\text{cm}^{-3}$ ) and indices  $\alpha_1$  below, and  $\alpha_2$  above the break Lorentz factor  $\gamma_{e,\text{break}}$ .

The two previously-mentioned X-ray spectral hypotheses (assuming an intrinsic break or an additional absorption) have been considered as lower and upper limits for the synchrotron emission from the blob. In case A, the synchrotron peak energy corresponds to the observed X-ray break energy, while in case B, the synchrotron peak falls between UV and X-rays. Whereas in case A the emission from the blob cannot explain both the X-ray and optical/UV data, in case B the synchrotron component, together with the emission from the host galaxy, can reproduce the infrared to X-ray observations. In both cases, the historical radio data are not taken into account, as it is more likely that they are produced in the extended jet. In order to study how the evaluation of the *Fermi*/LAT slope (which depends on the low-energy threshold, as described in Sec. 3.1) affects the overall SED, the modelling has been performed for the two *Fermi*/LAT spectra evaluated above 300 MeV and 1 GeV. For simplicity, only the modelling of the SED with the *Fermi*/LAT spectrum evaluated above 1 GeV is presented in Fig. 7.

The minimum and maximum Lorentz factors of the electron distribution cannot be constrained by the data, and they have been fixed at  $\gamma_{e,\min} = 300$  and  $\gamma_{e,\max} = 5 \times 10^6$ . The index of the electron distribution after the break  $\alpha_2$  is completely constrained by the observed X-ray photon index above the break, and has been fixed at 4.0. The slope  $\alpha_1$  is constrained by the *Fermi*/LAT photon index (for the two cases, A and B) and by the optical/UV data points (only for case B), and it has been fixed at 2.2 and 2.0 for a *Fermi*/LAT spectrum evaluated above 300 MeV and 1 GeV, respectively.

A good description of the SED can be obtained assuming an angle to the line of sight  $\theta = 1^\circ$  and a Doppler factor  $\delta = 30$ , corresponding to a bulk Lorentz factor of 16. The other free parameters ( $B$ ,  $R$ ,  $\gamma_{e,\text{break}}$ ,  $K$ ) are different between the cases considered, and their values are indicated in Tab. 5, together with the evaluation of the electron energy density  $u_e = mc^2 \int d\gamma_e \gamma_e N(\gamma_e)$  and the magnetic energy density in the blob  $u_B = B^2/8\pi$ . The  $u_e/u_B$  value is higher in case A (intrinsic break, and higher synchrotron peak energy) than in case B (additional absorption effect, and lower synchrotron peak energy), reflecting the fact that the ratio between the inverse Compton and the synchrotron component is higher in the first case. The lower limit on the variability time-scale, evaluated for the emitting region size and the Doppler factor assumed in the modelling, roughly corresponds to 1 and 25 hours for the cases A and B, respectively, consistent with the variability time-scale observed by ATOM.

The difference between the *Fermi*/LAT spectra evaluated for different energy thresholds affects the evaluation of the electron-

distribution slope before the break ( $\alpha_1$ ), and, consequently, it induces a variation on the normalization factor  $K$  and on the break Lorentz factor  $\gamma_{e,\text{break}}$ , modifying the value of the electron energy density inside the emitting region.

In case A, the observed flux at low frequency (infrared to UV) cannot be explained by the emission of the blob. An additional component is required (not shown in Fig. 7), such as the emission from the extended jet, dominating the non-thermal continuum from radio to UV, and being responsible for the variability observed in ATOM data.

On the other hand, in case B, the low-frequency emission can be described by the blob-in-jet component plus the contribution from the host galaxy, with the former being at the origin of the observed optical variability.

It should be noted that, in this case, the UV flux is slightly underestimated. To better describe the data, the model would need a harder slope  $\alpha_1$  in apparent conflict with the GeV constraints derived from *Fermi*/LAT. However, the uncertainties (both statistical and systematic) on the evaluation of the GeV slope, as well as on the value of the second absorber in case B (the error on the  $E_{B-V}$  value used for the dereddening of the data is about 20%; this uncertainty has not been taken into account in the plotting of the SED), can still explain this discrepancy.

As mentioned above, the two cases discussed here (A and B) are best considered as lower and upper limits for the SSC blazar emission. The real scenario may be more complex and lie between these two limiting cases.

## 5. Conclusions

The blazar 1RXS J101015.9–311909 has been observed by H.E.S.S. between 2006 and 2010, leading to the discovery of its VHE emission with a significance of 7.1 standard deviations. The time-averaged VHE spectrum of this blazar is soft, with a photon index of  $\Gamma = 3.08 \pm 0.42_{\text{stat}} \pm 0.20_{\text{sys}}$  and a flux 0.8% of that of the Crab nebula. The detection has been made using more powerful analysis methods, which provide an enhanced sensitivity at lower energies. Observations at other wavelengths have been analysed in order to have a multi-band view of the SED of this AGN newly-detected in the VHE range. In particular, a careful analysis of the HE emission in *Fermi*/LAT data reveals a detection of this AGN at a significance level of about 8.2 standard deviations.

No detectable variability is seen in the available VHE (H.E.S.S.), HE (*Fermi*/LAT) or X-ray (*Swift*/XRT) datasets, the latter being the most constraining for the evaluation of the variability at the  $\approx 10^3$  s timescale of the X-ray observations that have been analysed. On the other hand, the optical data from ATOM, contemporaneous to the H.E.S.S. observations, vary in both the B and R filters. The fitted position of the VHE emission is consistent with the positions of the X-ray and radio sources.

The study of the SED implies that 1RXS J101015.9–311909 is an HBL with the usual double-peaked SED, where the high-energy bump is fully characterized thanks to the detection of the source in the H.E.S.S. and *Fermi*/LAT datasets. The physical origin of the spectral break observed in the X-ray spectrum cannot be firmly determined, and two hypotheses, one assuming an intrinsic break and another considering an additional absorption effect, have been presented. The corresponding X-ray spectra are considered as the lower and upper limits of the intrinsic blazar emission at that wavelength. The SED can be reproduced reasonably well using a stationary one-zone SSC model, with parameter values compatible with those commonly assumed for

<sup>12</sup> For a justification of the use of this hypothesis see, for example, Kirk et al. (1998).



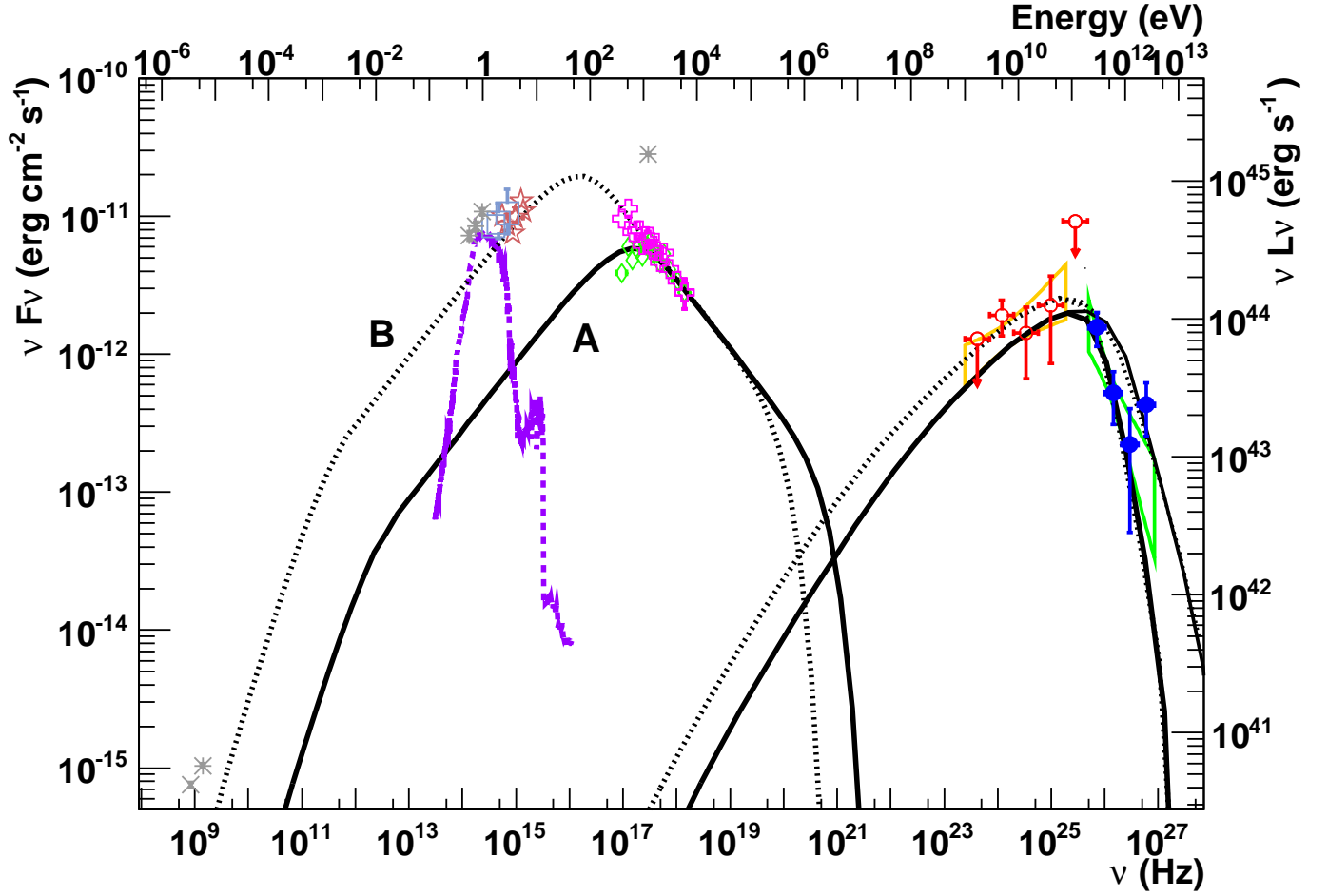


**Fig. 7.** Spectral energy distribution of 1RXS J101015.9–311909. The H.E.S.S. spectrum is represented by the green bow-tie at the highest energies. The measured *Fermi*/LAT spectrum above 1 GeV is represented by the orange full bow-tie, while the binned spectral points or upper limits are shown with empty circles (see Sec. 3.1 for details). The *Swift*/XRT spectrum in case A is shown with green diamonds, while case B is represented with pink crosses. NED database archival data are shown with grey asterisks, while the grey cross represents the flux measured by the SUMSS radio survey (see Sec. 1). *Swift*/UVOT data are shown with light-red stars; ATOM data are shown with light-blue squares. Deabsorbed infrared-to-UV data are plotted for case B only to avoid cluttering. The total SSC emission model (including absorption by the EBL) in case A is represented by the solid line, while the modelling in case B is represented by the dashed line. The intrinsic emission models (corrected for EBL absorption) are presented by the thinner lines at higher VHE flux. A template of a spectrum of a giant elliptical galaxy is also shown in the plot by the dashed purple line in the optical range.

relativistic jets. However, if the origin of the X-ray break is intrinsic, the model requires another component (most likely the emission from the extended jet) in order to describe optical and UV data.

Current uncertainties on the intrinsic X-ray spectrum, together with the non-simultaneity of the infrared to UV data, remain limiting factors for a realistic modelling of the low-energy bump. Future simultaneous multi-wavelength observations are required in order to determine whether optical/UV and X-ray photons are produced in the same emitting region, thus constraining the origin of the observed X-ray break.

The high-energy part of the SED turns out to be better constrained, with modelling only limited by the current uncertainty in the *Fermi*/LAT spectral index. Given the surveying strategy of *Fermi*/LAT, further data are expected to allow a more precise modelling of the source to be attained.

*Acknowledgements.* The support of the Namibian authorities and of the University of Namibia in facilitating the construction and operation of HESS is

gratefully acknowledged, as is the support by the German Ministry for Education and Research (BMBF), the Max Planck Society, the French Ministry for Research, the CNRS-IN2P3, and the Astroparticle Interdisciplinary Programme of the CNRS, the U.K. Science and Technology Facilities Council (STFC), the IPNP of the Charles University, the Polish Ministry of Science and Higher Education, the South African Department of Science and Technology and National Research Foundation, and by the University of Namibia. We appreciate the excellent work of the technical support staff in Berlin, Durham, Hamburg, Heidelberg, Palaiseau, Paris, Saclay, and in Namibia in the construction and operation of the equipment.

This research has made use of the NASA/IPAC Extragalactic Database (NED) which is operated by the Jet Propulsion Laboratory, California Institute of Technology, under contract with the National Aeronautics and Space Administration.

We acknowledge the use of public data from the *Swift* data archive. This research has made use of data and software provided by the *Fermi* Science Support Center, managed by the HEASARC at the Goddard Space Flight Center.

This publication makes use of data products from the Two Micron All Sky Survey, which is a joint project of the University of Massachusetts and the Infrared Processing and Analysis Center/California Institute of Technology, funded by the National Aeronautics and Space Administration and the National Science Foundation.

## References

- Abdo, A. A., Ackermann, M., Ajello, M., et al. 2010, *ApJS*, 188, 405
- Nolan, P. L., Abdo, A. A., Ackermann, M., et al. 2011, *ApJS*, 199, 31
- Aharonian, F. 2000, *New Astron.* 5, 377
- Aharonian, F. A., Akhperjanian, A. G., Bazer-Bachi, A. R., et al. 2006, *A&A*, 457, 899
- Aharonian, F., Akhperjanian, A. G., Bazer-Bachi, A. R., et al. 2006, *Nature*, 440, 1018
- Aharonian, F. A., Khargulyan, D., & Costamante, L. 2008, *MNRAS*, 387, 1206
- Atwood, W. B., Abdo, A. A., Ackermann, M., et al. 2009, *ApJ*, 697, 1071
- Becherini, Y., Djannati-Ataï, A., Marandon, V., Punch, M., & Pita, S. 2011, *Astrop. Phys.*, 34, 12, 858
- Bessell, M. S. 1990, *PASP*, 102, 1181
- Bock, D., Large, M. I., & Sadler, E. M. 1999, *AJ*, 117, 1578
- Burrows, D. N., Hill, J. E., Nousek, J. A., et al. 2005, *Space Sci. Rev.*, 120, 165
- Condon, J. J., Cotton, W. D., Greisen, E. W., et al., 1998, *AJ*, 115, 1693
- Costamante, L., & Ghisellini, G. 2002, *A&A*, 384, 56
- de Naurois, M., & Rolland L. 2009, *Astrop. Phys.*, 32, 231
- Dermer, C. D. & Schlickeiser, R. 1993, *ApJ*, 416, 458
- Dickey, J. M. & Lockman, F. J. 1990, *ARA&A*, 28, 215
- Feldman, G. J. & Cousins, R. D. 1998, *Phys. Rev. D* 57, 3873
- Fioc, M. & Rocca-Volmerange, B. 1997, *A&A*, 326, 950
- Franceschini, A., Rodighiero, G., & Vaccari, M. 2008, *A&A*, 487, 837
- Funk, S., Hermann, G., Hinton, J., et al. 2004, *Astrop. Phys.* 22, 285
- Gehrels, N., Chincarini, G., Giommi, P., et al. 2004, *ApJ*, 611, 1005
- Giommi, P., Piranomonte, S., Perri, M., & Padovani, P. 2005, *A&A*, 434, 385
- Hauser, M., Möllenhoff, C., Pühlhofer, G., et al. 2004, *Astronomische Nachrichten*, 325, 659
- Jarrett, T. H., Chester, T., Cutri, R., et al. 2000, *AJ*, 119, 2498
- Jenkins, E. B. & Savage, B. D. 1974, *ApJ*, 187, 243
- Katarzyński, K., Sol, H., & Kus, A. 2001, *A&A*, 367, 809
- Kirk, J. G., Rieger, F. M., & Mastichiadis, A. 1998, *A&A*, 333, 452
- Li, T. P., & Ma, Y. Q. 1983, *ApJ*, 272, 317
- Mannucci, F., Basile, F., Poggianti, B. M., et al. 2001, *MNRAS*, 326, 745
- Mannheim K., 1993, *A&A*, 269, 67
- Marscher, A. P. & Gear, W. K. 1985, *ApJ*, 298, 114
- Mattox, J. R., Bertsch, D. L., Chiang, J., et al. 1996, *ApJ*, 461, 396
- Meyer, M., Horns, D., & Zechlin, H. 2010, *A&A*, 523, 2
- Perlman, E. S., Madejski, G., Georgopoulos, M., et al., 2005, *ApJ*, 625, 727
- Piron, F., Djannati-Ataï, A., Punch, M., et al., 2001, *A&A*, 374, 895
- Piranomonte, S., Perri, M., Giommi, P., Landt, H., & Padovani, P. 2007, *A&A*, 470, 787
- Roming, P. W. A., Kennedy, T. E., Mason, K. O., et al. 2005, *Space Sci. Rev.*, 120, 95
- Roming, P. W. A., Koch, T. S., Oates, S. R., et al. 2009, *ApJ*, 690, 163
- Schlegel, D. J., Finkbeiner, D. P., & Davis, M. 1998, *ApJ*, 500, 525
- Vaughan, S., Edelson, R., Warwick, R. S., & Uttley, P. 2003, *MNRAS* 345, 1271
- Voges, W., Aschenbach, B., Boller, Th., et al. 1999, *A&A* 349, 389
- Young, P. J. 1976, *AJ*, 81, 807
- Cité, 10, rue Alice Domon et Léonie Duquet, 75205 Paris Cedex 13, France
- <sup>11</sup> Laboratoire Leprince-Ringuet, Ecole Polytechnique, CNRS/IN2P3, F-91128 Palaiseau, France
- <sup>12</sup> Institut für Theoretische Physik, Lehrstuhl IV: Weltraum und Astrophysik, Ruhr-Universität Bochum, D 44780 Bochum, Germany
- <sup>13</sup> Institut für Physik, Humboldt-Universität zu Berlin, Newtonstr. 15, D 12489 Berlin, Germany
- <sup>14</sup> LUTH, Observatoire de Paris, CNRS, Université Paris Diderot, 5 Place Jules Janssen, 92190 Meudon, France
- <sup>15</sup> LPNHE, Université Pierre et Marie Curie Paris 6, Université Denis Diderot Paris 7, CNRS/IN2P3, 4 Place Jussieu, F-75252, Paris Cedex 5, France
- <sup>16</sup> Institut für Astronomie und Astrophysik, Universität Tübingen, Sand 1, D 72076 Tübingen, Germany
- <sup>17</sup> Astronomical Observatory, The University of Warsaw, Al. Ujazdowskie 4, 00-478 Warsaw, Poland
- <sup>18</sup> Unit for Space Physics, North-West University, Potchefstroom 2520, South Africa
- <sup>19</sup> University of Durham, Department of Physics, South Road, Durham DH1 3LE, U.K.
- <sup>20</sup> Landessternwarte, Universität Heidelberg, Königstuhl, D 69117 Heidelberg, Germany
- <sup>21</sup> Oskar Klein Centre, Department of Physics, Stockholm University, Albanova University Center, SE-10691 Stockholm, Sweden
- <sup>22</sup> University of Namibia, Department of Physics, Private Bag 13301, Windhoek, Namibia
- <sup>23</sup> Laboratoire d'Astrophysique de Grenoble, INSU/CNRS, Université Joseph Fourier, BP 53, F-38041 Grenoble Cedex 9, France
- <sup>24</sup> Department of Physics and Astronomy, The University of Leicester, University Road, Leicester, LE1 7RH, United Kingdom
- <sup>25</sup> Instytut Fizyki Jądrowej PAN, ul. Radzikowskiego 152, 31-342 Kraków, Poland
- <sup>26</sup> Institut für Astro- und Teilchenphysik, Leopold-Franzens-Universität Innsbruck, A-6020 Innsbruck, Austria
- <sup>27</sup> Laboratoire d'Annecy-le-Vieux de Physique des Particules, Université de Savoie, CNRS/IN2P3, F-74941 Annecy-le-Vieux, France
- <sup>28</sup> Obserwatorium Astronomiczne, Uniwersytet Jagielloński, ul. Orła 171, 30-244 Kraków, Poland
- <sup>29</sup> Toruń Centre for Astronomy, Nicolaus Copernicus University, ul. Gagarina 11, 87-100 Toruń, Poland
- <sup>30</sup> School of Chemistry & Physics, University of Adelaide, Adelaide 5005, Australia
- <sup>31</sup> Charles University, Faculty of Mathematics and Physics, Institute of Particle and Nuclear Physics, V Holešovičkách 2, 180 00 Prague 8, Czech Republic
- <sup>32</sup> School of Physics & Astronomy, University of Leeds, Leeds LS2 9JT, UK
- <sup>33</sup> European Associated Laboratory for Gamma-Ray Astronomy, jointly supported by CNRS and MPG
- <sup>1</sup> Universität Hamburg, Institut für Experimentalphysik, Luruper Chaussee 149, D 22761 Hamburg, Germany
- <sup>2</sup> Laboratoire Univers et Particules de Montpellier, Université Montpellier 2, CNRS/IN2P3, CC 72, Place Eugène Bataillon, F-34095 Montpellier Cedex 5, France
- <sup>3</sup> Max-Planck-Institut für Kernphysik, P.O. Box 103980, D 69029 Heidelberg, Germany
- <sup>4</sup> Dublin Institute for Advanced Studies, 31 Fitzwilliam Place, Dublin 2, Ireland
- <sup>5</sup> National Academy of Sciences of the Republic of Armenia, Yerevan
- <sup>6</sup> Yerevan Physics Institute, 2 Alikhanian Brothers St., 375036 Yerevan, Armenia
- <sup>7</sup> Universität Erlangen-Nürnberg, Physikalisches Institut, Erwin-Rommel-Str. 1, D 91058 Erlangen, Germany
- <sup>8</sup> Nicolaus Copernicus Astronomical Center, ul. Bartycka 18, 00-716 Warsaw, Poland
- <sup>9</sup> CEA Saclay, DSM/IRFU, F-91191 Gif-Sur-Yvette Cedex, France
- <sup>10</sup> APC, AstroParticule et Cosmologie, Université Paris Diderot, CNRS/IN2P3, CEA/Irfu, Observatoire de Paris, Sorbonne Paris